Proceedings of the 26th International Conference on
Port and Ocean Engineering under Arctic Conditions
June 14-18, 2021, Moscow, Russia

Validation of inverse model for the estimation of ice-induced propeller axial loads

Brendon M. Nickerson[1], Anriëtte Bekker[1]

[1] Sound and Vibration Research Group, Stellenbosch University, Stellenbosch, South Africa

ABSTRACT

During March of 2017, the S.A. Agulhas II was at dry-dock for scheduled maintenance. Measurements were conducted on the port-side propulsion shaft in order to perform an operational modal analysis. These measurements are used alongside an inverse model of the shaft to investigate its axial properties. The inverse model transforms measured propulsion shaft thrust into axial propeller loads using modal superposition. Comparisons between the shaft design natural frequencies and those measured at dry-dock to the model's natural frequencies are used to validate the parameters of the model. It was found that the inclusion of thrust bearing stiffness and shaft bearing masses was necessary for accurate matching of the natural frequencies.

KEY WORDS: Inverse problem; Modal superposition; Propulsion shaft thrust; Ice-induced propeller load; Full-scale measurement

INTRODUCTION

The need for safe and efficient shipping in Arctic regions is increasing, due to expected increases in maritime transport in ice covered seas. The propulsion systems of vessels travelling in icy waters are exposed to ice-related impact loading in addition to hydrodynamic loading. This additional loading effects the safety and efficiency of vessel operation.

Structural failure of propulsion system components could occur due to either a loading condition exceeding the ultimate strength of the component, or due to a cyclic loading resulting in fatigue failure. Both of these loading conditions are exacerbated during propeller-ice interaction. This is due to increases in the maximum loading on the propeller blades during ice impacts.

In order to assess the propulsion system, it is necessary to quantify the loads it is subjected to. This can be done through direct measurements of the loading conditions. However, in the case of the propeller direct measurements can be difficult or infeasible due to sensors being damaged under the harsh operating conditions (Al-Bedoor, et al., 2006). Hence, it becomes necessary to measure elsewhere on the propulsion shaft, and make use of these measurements to determine the ice-induced propeller loads through an inverse problem.

The use of inverse problems to estimate the ice-induced propeller loads has been investigated in literature (Browne, et al., 1998; Ikonen, et al., 2014; De Waal, et al., 2018; Polic, et al., 2019;

Nickerson, 2021). Of these investigations, only Browne, et al. (1998) considered axial loads, while the others focused on the estimation of ice-induced propeller moments.

This paper presents an inverse model of the propulsion shaft of the S.A. Agulhas II (SAA II) that can be used to estimate axial or thrust loads on the propeller. The model is based on similar principles to one developed by Nickerson (2021) for estimation of propeller moments. The natural frequencies of the axial inverse model are compared to the design frequencies of the propulsion shaft, as well as to full-scale measurements taken on the shaft during dry-dock operations. This is done to validate whether the model is an accurate representation of the shaft axial response, and therefore suitable for the estimation of ice-induced axial propeller loads.

FULL-SCALE MEASUREMENTS

The SAA II, shown in Figure 1, was built by STX Finland in Rauma shipyard in 2012. Her hull was designed and strengthened according to DNV ICE-10 requirements and she was classified as Polar Ice Class PC-5. She is powered by four six-cylinder diesel engines, each generating 3 MW. The propulsion system consists of two diesel-electric powertrains each with a 4.5 MW electric motor driving four-bladed controllable pitch propellers. Table 1 provides the specifications for the SAA II.

Figure 1. The S.A. Agulhas II

The SAA II was in dry-dock during March of 2017. This was a scheduled maintenance event to be undertaken during the fifth year of the ship’s operations. This allowed for the replacement of components not easily maintained while the ship was afloat, for example the anodes preventing the rusting of the hull. The hull was also sandblasted and repainted, and the propeller blades inspected and maintained.

During these operations, an effort was made to conduct vibration measurements on the port side shaft-line in order to perform a modal analysis of the system. The data acquisition software used was LMS Test.Lab from Siemens (Siemens PLM Software, 2014), and the hardware consisted of two LMS SCADAS Mobile data acquisition units connected in a master-slave configuration, thirteen ICP accelerometers (PCB Piezotronics, 2021) and one impedance sensor (PCP Piezotronics, 2017) from PCB Piezotronics, and sledgehammer to provide excitation to the system. A limitation of this test was that a modal sledgehammer was not available.

Table 1. Specifications for the S.A. Agulhas II (Nickerson, 2021)

Gross tonnage	12 897 tons
Overall length	134.2 m
Length between perpendiculars	121.2 m
Breadth	22 m
Classification	DNV
Class notation	1A1 PC-5 / ICE-10
Built by	STX Finland
Location built	Rauma, Finland
Year built	2012
Diesel engine type	Wärtsilä 6L32
Electric motor type	Converteam N3 HXC 1120 LL8
MCR speed	140 rpm
MCR power	4.5 MW
MCR torque	307 kNm
Propeller manufacturer	Rolls-Royce
No. of propeller blades	4
Propeller diameter	4.3
Shaft characteristics	Direct drive
No. of motors / propellers	2 / 2

The shaft-line was instrumented with ICP accelerometers at three locations, each measuring the axial, perpendicular, and rotational vibrations. The measurement locations are highlighted in Figure 2. Figure 3(a) shows the instrumentation setup at measurement location 1, with similar setups used at the other locations. A single propeller blade was also instrumented with four ICP accelerometers; at the blade root, at the centre of the blade, and one each on the leading and trailing edges respectively. An impedance sensor was installed on the blade tip, in an attempt to measure the input force from the hammer excitation in addition to acceleration. This installation is shown in Figure 3(b).

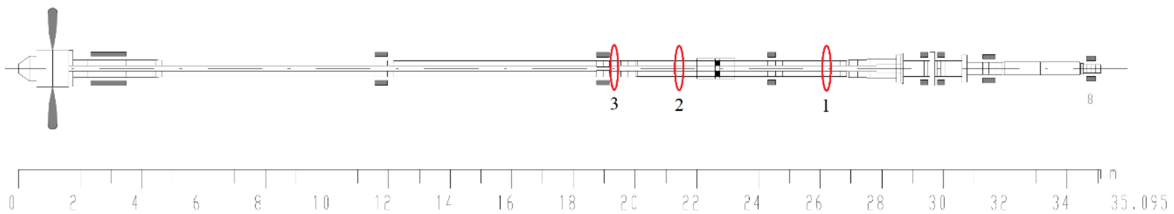

Figure 2. Propulsion shaft accelerometer measurement locations

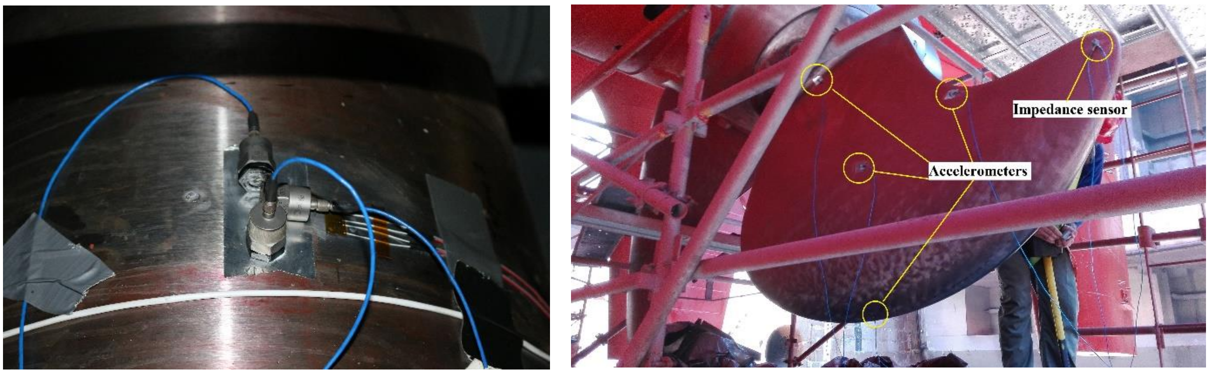

(a) (b)

Figure 3. Installed accelerometers: (a) on the shaft, and (b) on the blade

The tests were conducted by exciting the shaft-line system externally with the sledgehammer at various locations, including the blade tip, trailing edge, and propeller hub, in both axial and torsional directions to obtain vibration data. The power spectral density (PSD) plots of the measured vibrations are shown in Figure 4. Due to the limited excitation available for the large structure, the measurements on the shaft were not ideal. The measurements on the blades were much cleaner as they were nearer to the point of excitation.

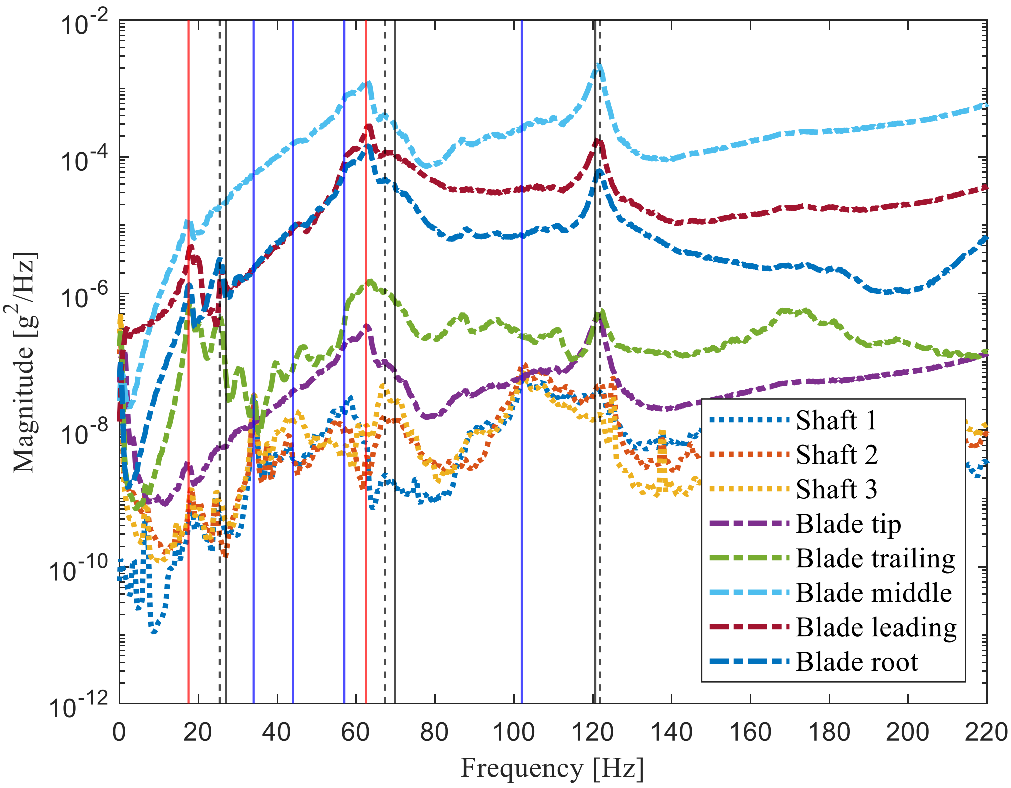

Figure 4. PSD of shaft and blade accelerometer measurements (duration: 60 seconds, sample rate: 2048 Hz, Block size: 8192, Window: Flat top, Overlap: 66%)

The first three natural frequencies of the shaft (27.0 Hz, 69.8 Hz, and 120.6 Hz), as determined by Rolls-Royce (Rolls-Royce AB, 2010) during design, are shown as solid black vertical lines in Figure 4. It can be seen that the blade and shaft exhibit frequencies near these, at 25.5 Hz, 67.3 Hz, and 121.8 Hz (dashed black vertical lines). Furthermore, the blade shows additional frequencies at 17 Hz and 62 Hz (red vertical lines) while the shaft has additional frequencies at 34 Hz, 44 Hz, 57 Hz, and 102 Hz (blue vertical lines). The additional frequencies may be due to local resonance phenomena. Differences between the design frequencies and those measured may also be due to the ship being tested out of water, without the additional mass, stiffness, and damping that the water would provide which is accounted for in the design. The percentage difference between the design frequencies and those measured at dry-dock are given in Table 2.

Table 2. Differences between design natural frequencies and frequencies measured at dry-dock

	Design	Dry dock	
	Freq.	Freq.	% Diff
f_1	27.0	25.5	**5.6**
f_2	69.8	67.3	**3.6**
f_3	120.6	121.8	**1.0**

INVERSE MODEL

For the model, a single shaft is considered between the propeller and thrust bearing. Figure 5 shows the model of the propulsion shaft with a differential element selected at a distance x along the shaft. The forces acting on the differential element are also shown, with $F(x,t)$ representing the internal propulsion shaft axial load and $F_d(x,t)$ the applied axial load. The propeller is located at $x = 0$ while the thrust bearing is situated at $x = L$. The model assumes a constant hollow circular cross section and consistent material properties along the length of the shaft. For the derivation of the model, an unknown distributed axial load is initially assumed to be applied along the length of the shaft.

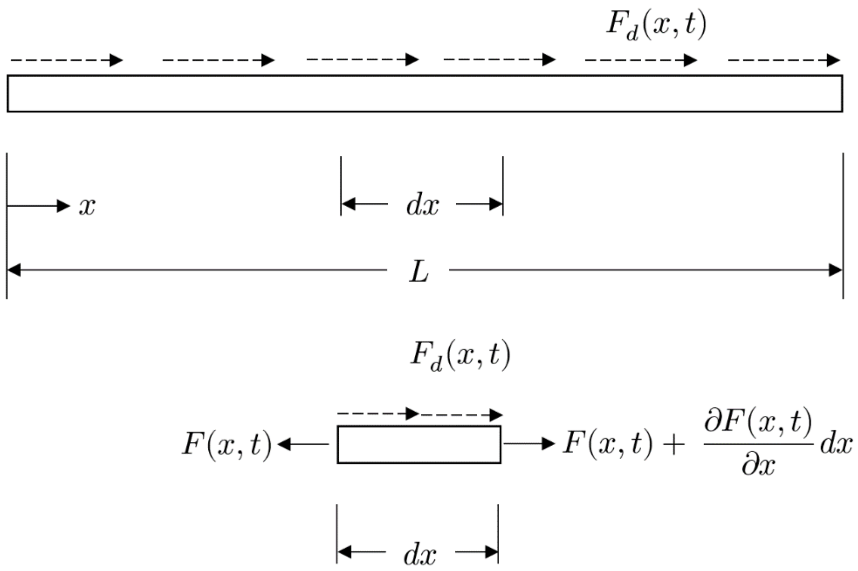

Figure 5. Propulsion shaft model for propeller axial load estimation

Newton's second law states that the sum of the applied forces on a body is equal to the rate of change of the momentum of that body (Inman, 2014). Equation 1 describes this equilibrium for the shaft.

$$\sum_i F_i = M\ddot{u} \tag{1}$$

where F_i represents the applied forces, M is the mass, and $\ddot{u}$ is the second derivative of the displacement in the x direction with respect to time.

Substituting the forces applied to the differential element in Figure 5 into Equation 1 gives Equation 2, describing the dynamic equilibrium of the differential element.

$$-F(x,t) + F_d(x,t)dx + \left(F(x,t) + \frac{\partial F(x,t)}{\partial x}dx\right) = \rho A(x)\frac{\partial^2 u(x,t)}{\partial t^2}dx \tag{2}$$

where ρ is the shaft material density, $A(x)$ is the cross sectional area of the shaft, $F(x,t)$ the internal axial load at distance x, and $F_d(x,t)$ the externally applied distributed axial load.

Rearranging Equation 2 and dividing all terms by dx gives Equation 3:

$$\rho A(x)\frac{\partial^2 u(x,t)}{\partial t^2} - \frac{\partial F(x,t)}{\partial x} = F_d(x,t) \tag{3}$$

The axial load in the shaft at x is related to the axial deflection at x by (Shames, 1997):

$$F(x,t) = EA(x)\frac{\partial u(x,t)}{\partial x} \tag{4}$$

with E the elastic modulus. Substitution of Equation 4 into Equation 3 yields:

$$\rho A(x)\frac{\partial^2 u(x,t)}{\partial t^2} - \frac{\partial}{\partial x}\left(EA(x)\frac{\partial u(x,t)}{\partial x}\right) = F_d(x,t) \tag{5}$$

Assuming a uniform cross section of the shaft, the area becomes constant and can factored out of the partial derivative with regards to x and Equation 5 becomes:

$$\rho A\frac{\partial^2 u(x,t)}{\partial t^2} - EA\frac{\partial^2 u(x,t)}{\partial x^2} = F_d(x,t) \tag{6}$$

Modal superposition is applied in order to transform the partial differential Equation 6 into a set of ordinary differential equations. The axial deflection $u(x,t)$ can be described as:

$$u(x,t) = \sum_{n=0}^{N} \varphi_n(x)q_n(t) \tag{7}$$

where N is the number of mode shapes used to describe the deflection of the shaft, $\varphi_n(x)$ are the mode shape values at x, and $q_n(t)$ are the corresponding modal coordinates as functions of time. The mode shapes are described by Equation 8 (Inman, 2014):

$$\varphi_n(x) = B_n \cos\left(\frac{n\pi x}{L}\right), \qquad n = 0,1,2,\dots,N \tag{8}$$

where the B_n are constant values determined from initial conditions. Substitution of Equation 7 into Equation 6 yields:

$$\rho A \sum_{n=0}^{N} \varphi_n(x)\ddot{q}_n(t) - EA \sum_{n=0}^{N} \varphi_n''(x) q_n(t) = F_d(x,t) \tag{9}$$

where the overdots on $q_n(t)$ and the primes on $\varphi_n(x)$ represent the second derivatives with respect to t and x respectively. Differentiating the mode shape with respect to x twice leads to:

$$\varphi_n'(x) = -B_n \left(\frac{n\pi}{L}\right) \sin\left(\frac{n\pi x}{L}\right) \tag{10}$$

$$\varphi_n''(x) = -B_n \left(\frac{n\pi}{L}\right)^2 \cos\left(\frac{n\pi x}{L}\right) = -\left(\frac{n\pi}{L}\right)^2 \varphi_n(x) \tag{11}$$

Substituting the second derivative of the mode shape, Equation 11, into Equation 9 gives:

$$\rho A \sum_{n=0}^{N} \varphi_n(x)\ddot{q}_n(t) + EA \sum_{n=0}^{N} \left(\frac{n\pi}{L}\right)^2 \varphi_n(x) q_n(t) = F_d(x,t) \tag{12}$$

The distributed axial load $F_d(x,t)$ applied to the shaft consists of a number of loads applied to the ends of the shaft, as seen in Figure 6. The propeller is modelled as an inertial load and the thrust load is applied at the propeller at x = 0. The thrust bearing is modelled as a spring load using the bearing stiffness (k_b) as spring constant.

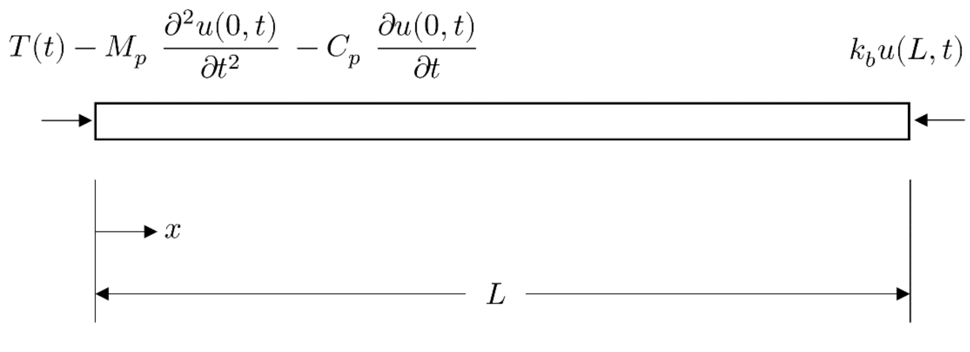

Figure 6. Axial loads applied to propulsion shaft model

The axial load $F_d(x,t)$ becomes:

$$F_d(x,t) = T(t)\delta(x-0) - M_p \frac{\partial^2 u(0,t)}{\partial t^2}\delta(x-0) - C_p \frac{\partial u(0,t)}{\partial t}\delta(x-0) - k_b u(L,t)\delta(x-L) \tag{13}$$

with T the propeller thrust load, M_p the mass of the propeller (and entrained water), C_p the hydrodynamic damping coefficient, and δ is the Dirac-delta function which states that for some constant value a:

$$\delta(x-a)=\begin{cases}1, & x=a\\ 0, & x\neq a\end{cases} \tag{14}$$

In order to remove the summations from Equation 12, the orthogonality of the mode shapes is used (Inman, 2014). This means that:

$$\int_0^L \varphi_m(x)\varphi_n(x)dx=\begin{cases}0, & n\neq m\\ L, & n=m=0\\ \dfrac{L}{2}, & n=m\end{cases} \tag{15}$$

Also note that:

$$\int_0^L \varphi_m(x)\delta(x-a)dx=\varphi_m(a)H(L-a) \tag{16}$$

with H the Heaviside step function:

$$H(L-a)=\begin{cases}0, & L<a\\ 1, & L\geq a\end{cases} \tag{17}$$

Equation 13 is substituted into Equation 12, multiplied through by $\varphi_m(x)$, and integrated over the length of the shaft. Taking note of the relationships in Equations 15 and 16, yields a separate ordinary differential equation for each mode shape n, Equation 18 for n = 0 and Equation 19 for n = 1, 2, …, N.

$$\begin{aligned}\rho AL\ddot{q}_0(t)=T(t)\varphi_0(0)-M_p\frac{\partial^2u(0,t)}{\partial t^2}\varphi_0(0)-C_p\frac{\partial u(0,t)}{\partial t}\varphi_0(0)\\ -k_bu(L,t)\varphi_0(L)\end{aligned} \tag{18}$$

$$\begin{aligned}\rho A\frac{L}{2}\ddot{q}_n(t)+EA\frac{(n\pi)^2}{2L}q_n(t)\\ =T(t)\varphi_n(0)-M_p\frac{\partial^2u(0,t)}{\partial t^2}\varphi_n(0)-C_p\frac{\partial u(0,t)}{\partial t}\varphi_n(0)\\ -k_bu(L,t)\varphi_n(L)\end{aligned} \tag{19}$$

Using modal superposition, Equation 7, once again for the deflection term in Equations 18 and 19 yields the final equations for each mode shape used in the model, Equation 20 for n = 0 and Equation 21 for n = 1, 2, …, N. :

$$\rho AL\ddot{q}_0(t) + M_p\varphi_0(0)\sum_{i=0}^{N}\varphi_i(0)\ddot{q}_i(t) + C_p\varphi_0(0)\sum_{i=0}^{N}\varphi_i(0)\dot{q}_i(t) + k_b\varphi_0(L)\sum_{i=0}^{N}\varphi_i(L)q_i(t) - T(t)\varphi_0(0) = 0 \quad (20)$$

$$\rho A\frac{L}{2}\ddot{q}_n(t) + M_p\varphi_n(0)\sum_{i=0}^{N}\varphi_i(0)\ddot{q}_i(t) + C_p\varphi_n(0)\sum_{i=0}^{N}\varphi_i(0)\dot{q}_i(t) + EA\frac{(n\pi)^2}{2L}q_n(t) + k_b\varphi_n(L)\sum_{i=0}^{N}\varphi_i(L)q_i(t) - T(t)\varphi_n(0) = 0 \quad (21)$$

For the inverse problem there are N equations, one for each mode shape, and $N + 1$ unknowns, the q_n terms and the propeller thrust load $T(t)$. Therefore, one extra equation is necessary and this comes from a thrust measurement taken on the shaft at $x = x_a$:

$$F(x_a, t) = EA\frac{\partial u(x_a, t)}{\partial x} = EA\sum_{n=0}^{N}\varphi_n'(x)q_n(t) \quad (22)$$

Equations 20 to 22 can then be written in matrix form, which facilitates their solution using a numerical time integration scheme:

$$\mathbf{M\ddot{q}} + \mathbf{C\dot{q}} + \mathbf{Kq} = \mathbf{F}, \qquad \mathbf{q} = \{q_0 \quad q_1 \quad q_2 \quad \dots \quad q_N \quad T\}^T \quad (23)$$

The solution is obtained using the JWH-α numerical time integration scheme. This scheme was first presented by (Jansen, et al., 1999) for the integration of the Navier-Stokes equations. It was recommended for use in structural dynamic problems by (Kadapa, et al., 2017), who tested the method against time integrations schemes. It was shown that this method has improved numerical dissipation and dispersion properties when compared to other methods, and that it does not suffer from overshoot.

It should be noted that additional masses can be added to the propulsion shaft by projecting them onto the modal equations, similar to how the propeller mass was accounted for. This allows for the model to consider additional masses such as bearings or couplings. Similarly, additional damping or stiffness can be considered.

RESULTS AND DISCUSSION

The natural frequencies of the model were compared to the design values from Rolls-Royce AB (2010) and the dry-dock measurements. Three iterations of the model were considered to investigate the effect of additional parameters on the model.

The first iteration considered the thrust bearing as a fixed support, and thus there was no spring stiffness k_b. Instead, $u(L,t) = 0$ was introduced as a boundary condition, resulting in different mode shapes. The derivation of the model is the same as that presented previously, while using the mode shape below:

$$\varphi_n(x) = B_n \sin\left(\frac{(2n-1)\pi(L-x)}{2L}\right), \qquad n = 0,1,2,\dots,N \tag{8}$$

The second iteration of the model is that discussed in the previous section. The thrust bearing is modelled as a spring support, using the stiffness value provided by the manufacturer. The third iteration also treats the thrust bearing as a spring support. In addition, the masses of the thrust bearing, stern tube bearings, and shaft coupling were modelled. The parameters for the models are provided in Table 3.

Table 3. Parameters for numerical model (Rolls-Royce AB, 2010)

Parameter	Value
Propeller mass	13 427 kg
Shaft outer diameter	0.5 m
Shaft inner diameter	0.175 m
Shaft length	28.54 m
Shaft elastic modulus	210 x 10^9 Pa
Shaft density	7 850 kg/m^3
Thrust bearing stiffness	5.0 x 10^9 N/m
Thrust bearing mass	5 850 kg
Thrust shaft mass	4 740 kg
Aft stern tube bearing mass	907 kg
Middle stern tube bearing mass	319 kg
Fore stern tube bearing mass	341 kg
Shaft coupling mass	1 400 kg

The natural frequencies of the models are compared to the design frequencies and those measured at dry-dock in Table 4. It can be seen that treating the thrust bearing as an ideal fixed support results in the largest disagreement between the model frequencies, and the design/measured frequencies. Introducing the bearing stiffness and the additional masses leads to a more accurate model. This suggests that it is import to account for all the mass and stiffness in the propulsion shaft system in order to produce an accurate axial model. This is contrary to the torsional case as it was found by Nickerson (2021) that a similar inverse model for propeller moment estimation only needed to consider the shaft, propeller, and motor inertias. The bearing inertias were not necessary to achieve a similar frequency response, and including them resulted in only minor increases in accuracy.

It can be seen from Table 4 that the difference in natural frequency, especially the second and third modes, is still significant by the third iteration of the model. This is likely due to additional mass and stiffness that is not taking into account by the model. Specifically, the model assumes a shaft of constant hollow cross section. However, the actual shaft has a number of outer and inner diameter changes along its length, resulting in a cross sectional area that varies along *x*. Towards both ends of the shaft, the area increases resulting in additional mass which would further reduce the natural frequencies of the model.

Table 4. Comparison of natural frequencies between design, dry-dock measurements, and inverse model

	Model with fixed support			Model with spring support			Model with spring support and additional masses		
	Freq.	% Diff Design	% Diff Dry-dock	Freq.	% Diff Design	% Diff Dry-dock	Freq.	% Diff Design	% Diff Dry-dock
f_1	31.7	**17.4**	**24.3**	26.9	**0.4**	**5.5**	26.2	**2.9**	**2.8**
f_2	106.2	**52.2**	**57.8**	89.4	**28.1**	**32.8**	78.6	**12.6**	**16.8**
f_3	190.9	**58.3**	**56.7**	164.5	**36.4**	**35.1**	135.1	**12.0**	**10.9**

CONCLUSIONS

An inverse model of the SAA II Propulsion shaft for the estimation of axial or thrust propeller loads has been developed and presented. The intended use for the model is the estimation of ice-induced propeller axial loads. To determine its suitability to this application, the model has been investigated in terms of its frequency response.

The natural frequencies of the model have been compared to the design specifications and measurements conducted in dry-dock. It was found that the model could be made more accurate by considering the effects of all additional masses and stiffness, other than just the shaft and propeller.

The model is already showing sufficient accuracy with regards to the first natural frequency. Thus, the model may be used to estimate propeller axial loads should the shaft response be dominated by the first mode. Full-scale measurements of the shaft axial response to ice impacts on the propeller blades may be used to verify whether this mode is dominant.

Future research should consider modelling the shaft with varying cross sectional area, as accounting for the full mass of the shaft should lead to a more accurate model. Additionally, bearing lubrication stiffness and damping may be accounted for.

ACKNOWLEDEMENTS

The financial assistance of the South African National Research Foundation through the South African National Antarctic Programme (Ref.: SNA170420228015, Grant No.: 110737) is gratefully acknowledged.

REFERENCES

Al-Bedoor, B. O., Aedwesi, S. & Al-Nassar, Y., 2006. Blades condition monitoring using shaft torsional vibration signals. *Journal of Quality in Maintenance Engineering,* 12(3), pp. 275-293.

Browne, R. P., Revil, C. R., Ritch, A. R. & Keinonen, A. J., 1998. Propeller design load model. *Transport Canada Publication - TP 13243E, Institute for Marine Dynamics, National Research Council Canada.*

De Waal, R. J. O., Bekker, A. & Heyns, P. S., 2018. Indirect load case estimation of ice-induced moments from shaft line torque measurements. *Cold Regions Science and Technology,* Volume 151, pp. 237-248.

Ikonen, T., Peltokorpi, O. & Karhunen, J., 2014. Inverse ice-induced moment determination on the propeller of an ice-going vessel. *Cold Regions Science and Technology,* Volume 112.

Inman, D. J., 2014. *Engineering Vibration.* 4th ed. Harlow: Pearson Education Limited.

Jansen, K., Whiting, C. & Hulbert, G., 1999. A generalised-a method for integrating the filtered Navier-Stokes equations with a stabilized finite element method. *Computer Methods in Applied Mechanics and Engineering,* Volume 190, pp. 305-320.

Kadapa, C., Dettmer, W. G. & Peric, 2017. On the advantages of using the first-order generalised-alpha scheme for structural dyanmic problems. *Computers and Structures,* Volume 193, pp. 226-238.

Nickerson, B. M., 2021. *Inverse models for ice-induced propeller moments on a polar vessel,* PhD Thesis: Stellenbosch University.

PCB Piezotronics, 2021. *ICP Accelerometer Model 333B32 Specifications.* [Online]
Available at: https://www.pcb.com/products?m=333b32
[Accessed 26 03 2021].

PCP Piezotronics, 2017. *Mechanical Impedance Sensor Model 288D01 Specifications.* [Online]
Available at:
https://www.pcb.com/contentstore/docs/PCB_Corporate/Vibration/Products/Specsheets/288D01_J.pdf
[Accessed 26 03 2021].

Polic, D., Ehlers, S. & Æsoy, V., 2019. Inverse modeling approach for transformation of propeller shaft angular deformation and velocity to propeller torque load. *Marine Structures,* Volume 67.

Rolls-Royce AB, 2010. Axial vibration calculation. *Report SA1091.*

Shames, I. H., 1997. *Engineering Mechanics: Statics and Dynamics.* 4th ed. Upper Saddle River: Prentice Hall.

Siemens PLM Software, 2014. *LMS Test.Lab, Powering testing productivity.* [Online]
Available at: https://www.dta.com.tr/pdf/brosur/siemens_lms/Siemens-PLM-LMS-Test-Lab_brosur.pdf
[Accessed 26 03 2021].